

Constraining the axiverse with reionization

Ziwen Yin,^{1,2,*} Hanyu Cheng,^{1,3,†} Eleonora Di Valentino,^{3,‡}
Naomi Gendler,^{4,§} David J. E. Marsh,^{2,¶} and Luca Visinelli^{5,6,**}

¹*Tsung-Dao Lee Institute & School of Physics and Astronomy, Shanghai Jiao Tong University, Shanghai 201210, China*

²*Theoretical Particle Physics and Cosmology, King's College London, Strand, London, WC2R 2LS, United Kingdom^{††}*

³*School of Mathematical and Physical Sciences, University of Sheffield, Hounsfield Road, Sheffield S3 7RH, United Kingdom^{††}*

⁴*Jefferson Physical Laboratory, Harvard University, Cambridge, MA 02138, USA*

⁵*Dipartimento di Fisica “E.R. Caianiello”, Università degli Studi di Salerno,
Via Giovanni Paolo II, 132 - 84084 Fisciano (SA), Italy*

⁶*Istituto Nazionale di Fisica Nucleare - Gruppo Collegato di Salerno - Sezione di Napoli,
Via Giovanni Paolo II, 132 - 84084 Fisciano (SA), Italy*

(Dated: July 8, 2025)

Axions that couple to electromagnetism are produced in the early Universe by, among other channels, freeze-in via the Primakoff process. For sufficiently large axion masses, the same coupling causes the axions to decay into two photons, which subsequently ionize the intergalactic medium. If this decay occurs in the redshift range $20 \lesssim z \lesssim 1100$, then the contribution to the cosmic microwave background optical depth τ_{reio} can lead to a conflict with observations, excluding models with sufficiently strongly coupled, heavy axions and high reheating temperatures, T_{reh} . Using large ensembles of explicit type IIB string theory models with up to $h^{1,1} = 100$ axions, we compute the full cosmic reionization history caused by the decays of multiple axions. We compare this to the posterior on the high- z component of τ_{reio} derived from model-independent constraints on the ionization state of the Universe, obtained in a full *Planck* analysis presented in a companion paper. For $h^{1,1} = 20, 50, 100$, we find that approximately 15%, 15%, and 10% of the models in the ensemble prefer $T_{\text{reh}} \lesssim 10^{10}$ GeV at 95% CL. We provide a publicly available code at: github.com/ZiwenYin/Reionization-with-multi-axions-decay, which computes the reionization history for arbitrary ensembles of decaying axions. Our analysis opens the door for future large-scale work studying the preference for low-temperature reheating in models with multiple axions.

I. INTRODUCTION

The idea that a fundamental pseudoscalar could constitute dark matter (DM) has its origins in the Peccei–Quinn (PQ) solution to the strong-CP problem in QCD [1, 2]. The spontaneous breaking of this symmetry gives rise to a pseudo-Nambu–Goldstone boson known as the QCD axion [3, 4]. Notably, the QCD axion not only solves the strong-CP problem but also emerges as a compelling DM candidate, provided it is produced through non-thermal mechanisms, such as vacuum misalignment, that allow it to remain cold and non-relativistic well before the epoch of recombination [5–7] (for reviews, see Refs. [8–11]). While thermal production via interactions with the Standard Model plasma is also possible, it typically leads to hot or warm relics and is therefore only viable for sufficiently heavy and weakly interacting axion-like particles or axions [12–14]. Such heavy axions that are abundantly produced by thermal processes are, however, unstable to decay into photons. Thus, thermally

produced axions are subject to strong constraints on their parameter space [13, 15–19].

String theory compactifications are known to give rise to a large number of axions in low-energy effective field theories (EFTs) [20–22], spanning a wide range of masses, known as an *axiverse* [23–25]. The phenomenology of such theories can be rich. In particular, Ref. [23] identified cosmic microwave background (CMB) birefringence, suppressed clustering of DM, black hole superradiance, and axion decays as four key areas of interest. Due to advances in computational algebraic geometry [26, 27], it has recently become possible to explore how this phenomenology manifests across large ensembles of explicit compactifications of type IIB string theory. So far, this technology has been deployed to test string theory using suppressed dark matter clustering [28], black hole superradiance [29], the strong-CP problem [30], birefringence [29, 31], and to compute the QCD axion mass as a function of topology [31–33]. In this work, we use the method to construct EFTs outlined in Ref. [31] and subject these models to the rigorous statistical testing we developed in Ref. [34] from the effects of axion decays on the CMB optical depth.

Using approximate formulae and rough comparisons to astrophysical limits, it was observed in Ref. [31] that freeze-in production followed by decay of axions, constrained by the CMB optical depth and other observables [17, 35], seems to place string theory in tension with models of high-temperature reheating. It is the purpose of the present work to place this observation on firm foot-

* ziwenyin@sjtu.edu.cn

† chenghanyu@sjtu.edu.cn

‡ e.divalentino@sheffield.ac.uk

§ ngendler@g.harvard.edu

¶ david.j.marsh@kcl.ac.uk

** lvisinelli@unisa.it

†† ZY and HC contributed equally to this work

ing with rigorous calculation. Our methodology is the following:

- Compute the freeze-in abundance of each individual axion species, using the accurate fitting formulae of Ref. [36] (where it was verified that inter-axion interactions can be neglected).
- Compute the full reionization history of the intergalactic medium caused by all¹ axion decays simultaneously, accurately following the baryon temperature, and using energy transfer functions computed separately using DARKHISTORY [37].
- Compare the resulting contribution to the CMB optical depth to a model-independent posterior on the high- z ionization state derived in a full *Planck* analysis, as presented in Paper I [34].
- Repeat, varying the reheat temperature T_{reh} to determine the maximum allowed value.

We perform this analysis for an ensemble of string theory models described below.

This paper is organized as follows. In Sec. II, we review the theoretical framework for axions in string theory, including their production and decay channels. In Sec. III, we compute the ionization history of the intergalactic medium resulting from axion decays. We present our model-independent reconstruction of the high-redshift optical depth in Sec. IV, and compare it to predictions from single-axion models in Sec. V. In Sec. VI, we use this framework to constrain ensembles of string theory models. Finally, we summarize our conclusions in Sec. VII. The code developed for computing the reionization history with arbitrary populations of decaying axions is publicly available at: github.com/ZiwenYin/Reionization-with-multi-axions-decay, and can be extended to other decaying dark matter scenarios by modifying the relic abundance input.

II. AXION COSMOLOGY

A. Axions in string theory

Axions arise in the closed-string (gravitational) sector of string theory due to dimensional reduction of p -form gauge fields (see Ref. [38] for open-string axions). Consider type IIB string theory, described below the string scale by ten-dimensional supergravity, which contains a 4-form field C_4 with field strength $F_5 = dC_4$ and action:

$$S_{10D} = \int F_5 \wedge \star F_5. \quad (1)$$

Taking the spacetime manifold to be $M = \mathcal{M}^{3+1} \times X_6$, where \mathcal{M}^{3+1} is Minkowski space with coordinates x , and X_6 is a Calabi–Yau (CY) orientifold with coordinates y , then the low-energy effective field theory below the Kaluza–Klein scale of X_6 has $\mathcal{N} = 1$ supersymmetry [39]. The CY topology is partially specified by the Hodge numbers $h^{1,1}$ and $h^{2,1}$, which are split into even and odd components by the orientifold action. For simplicity, consider only the case $h^{1,1} = h_+^{1,1}$, which leads to no orientifold-odd axions (see e.g. Ref. [40]).

Taking all four indices of C_4 to point along the coordinates in X_6 , vacuum solutions of the equations of motion for C_4 can be found by decomposing in terms of harmonic 4-forms $\omega_i(y)$:

$$C_4 = \sum_i a_i(x) \omega_i(y). \quad (2)$$

Under these model-building assumptions, the index i in Eq. (2) runs from 1 to $h_+^{1,1}$, and the fields $a_i(x)$ give rise to all $h_+^{1,1}$ axions in the closed-string sector. Dimensionally reducing the 10D action leads to a 4D action for the axions:

$$S_{4D} = \int K_{ij} da_i \wedge \star da_j, \quad (3)$$

where K_{ij} is the Kähler metric, which can be derived from the Kähler potential $\mathcal{K} = -\ln \mathcal{V}$, where \mathcal{V} is the volume of X_6 in string units.

The harmonic 4-forms ω_i are associated to divisors (four-dimensional closed cycles) of X_6 , the volumes of which are specified by the moduli fields ϱ_i , which arise from dimensional reduction of the Einstein–Hilbert term, and form chiral superfields paired with the axions a_i . We will assume that the moduli are stabilized [41, 42] with large masses at a point in the “stretched Kähler cone” of X_6 : the region where all ϱ_i have volume larger than one in string units and the EFT is under control [26].

The axions are massless to all orders in perturbation theory. They acquire mass due to non-perturbative effects; in particular, we consider Euclidean D3-branes wrapping the divisors of X_6 , which lead to the scalar potential:

$$V = - \sum_{\alpha} \Lambda_{\alpha}^4 \cos(Q_{\alpha i} a_i + \delta_{\alpha}), \quad (4)$$

where $\Lambda_{\alpha}^4 \propto e^{-2\pi Q_{\alpha i} \varrho_i}$ (see Ref. [28] for a complete definition), $Q_{\alpha i}$ are integer charges specified by the topology of X_6 (in the prime toric basis where the kinetic term is K_{ij}), and δ_{α} are phases. In addition, we include the instanton potential for QCD; QCD is itself modeled as described below. For the effects of the phases, see the discussions in Refs. [29–31].

The EFT for the axions can now be found by expanding the cosine potential, and diagonalizing the Kähler metric and mass matrix to give canonically normalized fields defined by a mass m_i^2 and decay constant f_i^2 . The Kähler metric terms, which specify f_i^2 , scale as

¹ In practice, we limit to a maximum of ten decaying axions.

M_{Pl}^2/o_i^2 , with $M_{\text{Pl}}^2 = 1/(8\pi G_N)$ the four-dimensional Planck mass, while the terms in the mass matrix scale as $e^{-2\pi\varphi_i}$. Thus, variations in the values set for the moduli lead to relatively mild hierarchies in the decay constants, which remain at high scales, while the axion masses become spread out over many decades [29]. Due to the hierarchies in the scales Λ_α , it is possible to perform the diagonalization and canonical normalization of the axions perturbatively and efficiently [30, 31]. It was found in Ref. [26] that the requirement of having all divisor volumes greater than unity has the effect that, as $h^{1,1}$ increases—thus adding more divisors and more constraints—this forces the volume to become larger and some divisors to be very large. This has the effect on the EFT that axion masses and, more importantly, decay constants fall as more axions are added to the spectrum.

In order to search for evidence of axions beyond their gravitational interactions, we must compute their couplings to the Standard Model. In type IIB string theory, the Standard Model gauge group can be realized by wrapping D7-branes on divisors in X_6 . We use the toy model described in Ref. [31] and simply select random prime toric divisors for this purpose (which divisors are suitable in reality is related to the choice of orientifold and the application of Gauss’ law to the branes).

We choose one divisor to host the $SU(3)_c$ part of the Standard Model, and either the same divisor or an intersecting divisor to host the $SU(2)_L \times U(1)_Y$ part. We then select a point in the stretched Kähler cone, given a homogeneous dilation of the tip, such that the divisor hosting $SU(3)_c$ has volume 40 in string units, giving a gauge coupling $\alpha = 1/40$ at the Kaluza–Klein scale, consistent with the known renormalization group running in the Standard Model assuming high-scale (or no) supersymmetry. We also demand that the $SU(2)_L \times U(1)_Y$ divisor have volume less than 120, such that renormalization group running of the electroweak sector is not drastically altered.

As described in Refs. [30, 31], it is now possible to identify the QCD axion [1, 3, 4] that solves the strong-CP problem (for reviews, see Refs. [8–11]), and to compute the couplings of all the axions to electromagnetism:

$$\mathcal{L}_{a\gamma\gamma} = -\frac{1}{4} \sum_i g_{a\gamma\gamma}^i \phi_i F_{\mu\nu} \tilde{F}^{\mu\nu}, \quad (5)$$

where $g_{a\gamma\gamma}^i$ is the coupling of the canonically normalised i -th axion mass eigenstate, ϕ_i to photons.

We construct CYs following Batyrev’s method [43] for 3-fold hypersurfaces in ambient toric varieties, which are themselves constructed from triangulations of reflexive polytopes in the Kreuzer–Skarke database [44]. This process is automated using CYTOOLS [27], which computes the triple intersection numbers necessary for the relevant computations and returns the Kähler metric and divisor volumes given a point in moduli space.²

To assess the effect of CY topology, we sample 50 polytopes and 10 triangulations of each for $h^{1,1} = 20, 50, 100$. For every CY thus constructed, we select every suitable prime toric divisor as a candidate to host QCD, as well as a random intersecting divisor for the electroweak sector. The point in moduli space is specified by Kähler parameters \vec{t} , which are given by $\lambda \vec{t}_0$, where \vec{t}_0 is the tip of the stretched Kähler cone and λ is chosen such that the QCD divisor takes volume 40 in string units. For the Kähler cone, we use \mathcal{K}_\cup , which approximates the true CY Kähler cone as a union of toric Kähler cones (see e.g. Ref. [29]). This improves on the calculation of Ref. [31], which used \mathcal{K}_V , the Kähler cone of the ambient variety. Since $\mathcal{K}_V \subset \mathcal{K}_\cup$, using the larger \mathcal{K}_\cup allows one to include more small divisors. \mathcal{K}_\cup is a better approximation to the true Kähler cone of the CY, and the additional small divisors available compared to \mathcal{K}_V allow a more representative sampling of the moduli space. Computational constraints limit using \mathcal{K}_\cup to smaller values of $h^{1,1} \lesssim 100$, and so we could not explore the largest value $h^{1,1} = 491$ as in Ref. [31].

B. Axion production and decay

The axion–photon coupling leads to axion production in the early Universe primarily through the Primakoff process, which dominates when axions couple to photons (we conservatively set the contribution from misalignment to zero). In this process, thermal photons scatter off charged particles in the Standard Model plasma, $q + \gamma \rightarrow q + a$, converting into axions in the presence of electromagnetic fields sourced by these charged particles. The same interaction governs axion decay to two photons, with decay rate:

$$\Gamma_{a \rightarrow \gamma\gamma} = \frac{m_a^3 g_{a\gamma\gamma}^2}{64\pi}, \quad (6)$$

where in this equation and in the following we refer to individual axions and for simplicity drop the subscript i labeling them. If the axion mass is sufficiently large, $m_a \gg 1$ eV, then the decay products leave astrophysical signatures and strongly constrain the axion parameter space. These processes are depicted in Fig. 1 for the Primakoff production (left) and particle decay (right). Here, we compute the decay temperature T_{decay} and the corresponding redshift z_{decay} using the methods outlined in Ref. [36].

Early studies of this phenomenology [13, 46] made the assumption that the axions came into thermal equilibrium in the early Universe, followed by freeze-out. In

in principle possible following Moritz [45], and implemented at scale in Ref. [28] at small $h^{1,1}$. We simply assume that a compatible orientifold with $h^{1,1} = h_+^{1,1}$ exists for the given polytope triangulation.

² We do not construct explicit orientifolds, although this is now

this case, constraints on $g_{a\gamma\gamma}$ are incredibly powerful, only allowing $g_{a\gamma\gamma} \ll M_{\text{Pl}}^{-1}$. However, the assumption of freeze-out is only valid if the reheating temperature (maximum thermalization temperature), T_{reh} , is larger than the freeze-out temperature of the dominant Primakoff interaction [13, 46]:

$$T_{\text{fo}} \approx 10^{16} \frac{\sqrt{g_*}}{g_Q} \left(\frac{10^{-16} \text{ GeV}^{-1}}{g_{a\gamma\gamma}} \right)^2 \text{ GeV}, \quad (7)$$

where g_* and g_Q are the relativistic and charged number of degrees of freedom in the plasma, respectively.

For lower reheating temperatures, $T_{\text{reh}} < T_{\text{fo}}$, axions are instead produced through freeze-in [47], rather than reaching thermal equilibrium. In this regime, the resulting axion abundance depends sensitively on the reheating temperature [16, 17, 36], with a minimum set by the “irreducible” contribution at big bang nucleosynthesis (BBN), $T_{\text{reh}} \gtrsim T_{\text{BBN}} \approx 5 \text{ MeV}$ (see e.g. Refs. [48, 49]), and a maximum at $T_{\text{reh}} \lesssim 10^{16} \text{ GeV}$, corresponding to the maximum temperature allowed in inflationary models, with the energy scale constrained by searches for primordial gravitational waves in the CMB [50].

The freeze-in energy density of axions produced from the Primakoff process can be parameterized as [51]

$$\begin{aligned} \rho_{\text{Prim}}(T \ll T_{\text{reh}}) &= A_{\text{Prim}} \frac{2.4 \times 10^{-8}}{\sqrt{g_*(T_{\text{reh}})}} \left(\frac{T_{\text{reh}}}{10 \text{ MeV}} \right) \left(\frac{g_{a\gamma\gamma}}{10^{-11} \text{ GeV}^{-1}} \right)^2 \\ &\times \left(\frac{a(T_{\text{reh}})}{a(T)} \right)^3 \left(\frac{m_a}{1 \text{ MeV}} \right) \left(\frac{n_{\text{eq}}(T_{\text{reh}})}{1 \text{ MeV}^3} \right) \text{ MeV}^4, \end{aligned} \quad (8)$$

where n_{eq} is the number density of axions in thermal equilibrium at $T = T_{\text{reh}}$. In the limit $m_a \ll T_{\text{reh}}$, the expression above simplifies to

$$\begin{aligned} \rho_{\text{Prim}}(T \ll T_{\text{reh}}) &= A_{\text{Prim}} \frac{2.4 \times 10^{-5}}{\sqrt{g_*(T_{\text{reh}})}} \frac{\zeta(3)}{\pi^2} \left(\frac{T_{\text{reh}}}{10 \text{ MeV}} \right)^4 \left(\frac{g_{a\gamma\gamma}}{10^{-11} \text{ GeV}^{-1}} \right)^2 \\ &\times \left(\frac{a(T_{\text{reh}})}{a(T)} \right)^3 \left(\frac{m_a}{1 \text{ MeV}} \right) \text{ MeV}^4, \end{aligned} \quad (9)$$

where the numerical coefficient A_{Prim} , which depends on m_a and T_{reh} , is computed in Ref. [36]. The resulting freeze-in fraction of decaying axion dark matter for $T \gg T_{\text{decay}}$ is then

$$\begin{aligned} \mathcal{F}_{\text{Prim}} &\equiv \frac{\rho_{\text{Prim}}}{\rho_{\text{DM}}} \\ &= \frac{3.4 \times 10^{-3} A_{\text{Prim}}}{\sqrt{g_*(T_{\text{reh}})}} \left(\frac{T_{\text{reh}}}{10 \text{ MeV}} \right) \left(\frac{g_{a\gamma\gamma}}{10^{-11} \text{ GeV}^{-1}} \right)^2 \\ &\times \left(\frac{m_a}{1 \text{ MeV}} \right). \end{aligned} \quad (10)$$

We have cross-checked the approximation in Eq. (10) by computing the full integral expression for the equilibrium

number density n_{eq} in Eq. (8), including the effects of thermal suppression. While this correction slightly modifies the result at low temperatures, the impact is minimal, as discussed further in Appendix A. The approximation used in Eq. (10) remains valid across the relevant parameter space.

A complementary freeze-in channel arises from the inverse decay process $\gamma + \gamma \rightarrow a$, with the resulting relic fraction given by

$$\begin{aligned} \mathcal{F}_{\text{Id}} &= A_{\text{Id}} \frac{1.42 \times 10^{-4}}{\sqrt{g_*(T')}} \left(\frac{g_{a\gamma\gamma}}{10^{-11} \text{ GeV}^{-1}} \right)^2 \left(\frac{m_a}{0.1 \text{ MeV}} \right)^2 \\ &\times \left(\frac{T'}{T_{\text{Id}}} \frac{4 \left(\frac{T_{\text{Id}}}{T'} \right)^2 - 1}{3^{3/2}} \frac{\coth(0.1 \frac{T_{\text{Id}}}{T'})}{\coth(0.1)} \right)_{T'=\min[T_{\text{Id}}, T_{\text{reh}}]}, \end{aligned} \quad (11)$$

where $T_{\text{Id}} \simeq 2.5 m_a$ is the inverse decay threshold, and A_{Id} is a phenomenological factor that solely depends on the axion mass [36]. In the region of interest, the contribution from e^+e^- annihilation is negligible. Finally, we define the total abundance of axions, \mathcal{F}_a , “as if the axion were stable” [17], as the sum of the freeze-in contributions from the Primakoff and inverse decay processes:

$$\mathcal{F}_a \simeq \mathcal{F}_{\text{Prim}} + \mathcal{F}_{\text{Id}}. \quad (12)$$

The above fitting formulae allow us to compute the fraction of would-be dark matter composed of axions before their decay, as a function of the axion mass m_a , the axion-photon coupling $g_{a\gamma\gamma}$, and the reheat temperature T_{reh} . This fraction serves as the input for the next stage of our analysis.

Note that it is implicitly assumed that such reheating is instantaneous, i.e. inflation ends at T_{reh} and there are no axions produced in the prior epoch. Similarly to neglecting the possible misalignment population of axions (which can be fine-tuned away), the assumption of instantaneous reheating leads to conservative constraints from the irreducible freeze-in population. Alternatively, one could consider explicit modified cosmologies [28, 52] or take the abundance as an independent free parameter with \mathcal{F}_a above giving the minimum [16].

III. IONIZATION OF THE INTERGALACTIC MEDIUM BY AXION DECAY

We first consider the ionization rate of our Universe between recombination and reionization, corresponding to the redshift range $10 \lesssim z \lesssim 1100$. The recombination epoch is mainly governed by the evolution of the ionization fraction X_e , defined as the ratio between the number densities of free electrons n_e and hydrogen nuclei n_H ,

$$X_e = \frac{n_e}{n_H}, \quad (13)$$

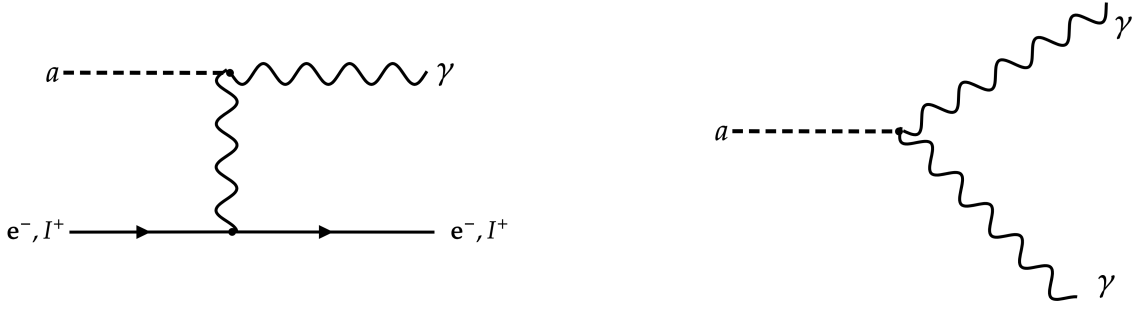


FIG. 1. Left: Axion production by the Primakoff process. Right: Axion to two photon decay.

and the baryon temperature T_b . More precisely, the differential equations describing the evolution of these quantities read [53, 54]

$$\begin{aligned} \frac{dX_e}{dz} &= \frac{C_H}{(1+z)H(z)} \left(-\beta_H(T_\gamma)(1-X_e)e^{\frac{-E_{H,2s1s}}{T_\gamma}} + X_e^2 n_H \alpha_H(T_b) \right) \\ &+ \frac{1}{n_H E_i} \frac{dE}{dV dz} \Big|_{\text{dep,ion}} + (1-C_H) \frac{1}{n_H E_{H,1s2p}} \frac{dE}{dV dz} \Big|_{\text{dep,exc}}, \\ (1+z) \frac{dT_b}{dz} &= 2T_b + \frac{8}{3} \frac{\rho_\gamma \sigma_T}{m_e H(z)} \frac{X_e}{1+f_{\text{He}}+X_e} (T_b - T_\gamma) \\ &- \frac{2}{3} \frac{1+z}{n_H(1+f_{\text{He}}+X_e)} \frac{dE}{dV dz} \Big|_{\text{dep,heat}}, \end{aligned} \quad (14)$$

where T_γ is the photon temperature, $H(z)$ is the Hubble parameter at redshift z , $E_{H,1s2s} = E_{H,1s2p} = 10.2$ eV is the energy difference between the 2s and 1s energy levels of the hydrogen atom, and $E_i = 13.6$ eV is the average ionization energy of hydrogen. The factor C_H gives the probability for an electron in the first excited state to transition to the ground state before being ionized [54]. Moreover, the evolution of T_b is influenced by the Thomson scattering cross section σ_T and the photon energy density ρ_γ , while the coefficients β_H and α_H appearing in the evolution of X_e correspond to photoionization and recombination rates, respectively.

For each energy deposition channel, labeled by “c”, with “ion” for ionization, “exc” for excitation, and “heat” for IGM heating, the energy deposition rate takes the form

$$\frac{dE}{dV dz} \Big|_{\text{dep,c}} = f_c(z) \frac{dE_{\text{inj}}}{dV dz}, \quad (16)$$

where $f_c(z)$ is the redshift-dependent efficiency for the channel “c”. The efficiency function $f_c(z)$ is obtained using the DARKHISTORY code [37], and we precompute it for our analysis. To simplify the computation, we adopt the beyond on-the-spot assumption [35], in which energy injected at redshift z is assumed to be deposited instantaneously. However, rather than assuming a constant efficiency, we retain the full redshift-dependent form of $f_c(z)$ as computed numerically.

The energy injection rate due to axion decays is given by [55]

$$\frac{dE_{\text{inj}}}{dV dz} = \frac{\Gamma_{a \rightarrow \gamma\gamma} e^{-\Gamma_{a \rightarrow \gamma\gamma} t(z)}}{(1+z)H(z)} \mathcal{F}_a \rho_c \Omega_{\text{DM}} (1+z)^3, \quad (17)$$

where $\Gamma_{a \rightarrow \gamma\gamma}$ is the axion decay rate defined in Eq. (6), \mathcal{F}_a is the DM fraction in axions prior to decay in Eq. (12), Ω_{DM} is the present DM density fraction, and ρ_c is the critical density today. We also define the total number density of hydrogen, including both neutral H and ionized H^+ , as a function of photon temperature T_γ :

$$n_H = n_e + n_p = 3.1 \times 10^{-8} \eta_{10} (T_\gamma/T_{\gamma 0})^3 \text{ cm}^{-3} \quad (18)$$

where $\eta_{10} = 10^{10} n_b/n_\gamma \simeq 6.1$ is the baryon-to-photon ratio [56], n_b is the baryon number density, and $T_{\gamma 0} \approx 2.7$ K is the present-day photon temperature. This leads to the photon temperature at redshift z as:

$$T_\gamma = T_{\gamma 0} (1+z). \quad (19)$$

The reionization era, corresponding to redshifts $z \lesssim 10$, is modeled using the tanh parametrization, see e.g. Ref. [57]. This describes the reionization of hydrogen and singly ionized helium as:

$$X_{\text{rei}} = \frac{1+f_{\text{He}}}{2} \left[1 + \tanh \left(\frac{(1+z_{\text{re}})^{3/2} - (1+z)^{3/2}}{(3/2)(1+z)^{1/2} \Delta z} \right) \right], \quad (20)$$

where $z_{\text{re}} = 6.1$, $\Delta z = 0.5$ and the helium-to-hydrogen number density ratio is given by

$$f_{\text{He}} = \frac{n_{\text{He}}}{n_H} = \frac{Y_p}{4(1-Y_p)}, \quad (21)$$

with Y_p denoting the primordial helium mass fraction. In this model, the full ionization history is expressed as the sum of the contributions from recombination and reionization:

$$X_e^{\text{tot}}(z) = X_e(z) + X_{\text{rei}}(z). \quad (22)$$

To illustrate the impact of axion decays on the ionization history, Fig. 2 shows the evolution of the ionization fraction in a model with a single axion-like particle of mass $m_a = 10^5$ eV and photon coupling $g_{a\gamma\gamma} =$

$6 \times 10^{-13} \text{ GeV}^{-1}$, assuming a low reheating temperature $T_{\text{reh}} = 5 \text{ MeV}$. The axion population, comprising a small fraction $\sim 10^{-7}$ of the DM, decays after recombination and induces substantial ionization of the intergalactic medium at high redshift, compared to the standard cosmological history (black line). This early energy injection results in an optical depth $\tau_{\text{reio}} \approx 1.92$, which is in strong tension with observational limits.

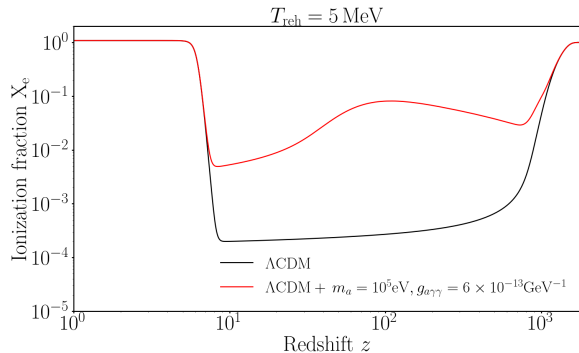


FIG. 2. **Single axion case.** Ionization fraction in the ΛCDM scenario (black line), compared to a model with one additional axion component, assuming instantaneous energy injection with the “beyond on-the-spot” assumption and using the full energy deposition efficiency function provided by DARKHISTORY. The axion, constituting a fraction $\approx 10^{-7}$ of the DM, decays at redshift $z_{\text{decay}} < 1100$, leading to efficient ionization of the intergalactic medium and a CMB optical depth $\tau_{\text{reio}} \approx 1.92$.

In the string axiverse, multiple axions with hierarchically different masses and decay constants can lead to distinct episodes of energy injection in the post-recombination Universe. To study scenarios with a large number of axions, we focus on a mass window ranging from 10^5 eV to 10^{10} eV , and select up to 10 axions per model within this window to compute the cumulative energy injection. Figure 3 shows example energy injection histories from the models presented in Ref. [31], sampled from an ensemble of CYs with $h^{1,1} = 50$. The selected cases include models with between one and six axions in the specified mass window. In this ensemble, the maximum number of axions found in the mass window for any given model is 8.

Figure 4 illustrates the ionization history $X_e(z)$ resulting from a representative string axion model within the $h^{1,1} = 50$ ensemble. Details for the computations are similar to those outlined for Fig. 2. The selected string axion model includes two axions within the mass range relevant for contributions to the CMB optical depth: one with mass $m_a^{(1)} = 8.27 \text{ GeV}$ and photon coupling $g_{a\gamma\gamma}^{(1)} = 1.87 \times 10^{-20} \text{ GeV}^{-1}$, and a second with $m_a^{(2)} = 0.72 \text{ GeV}$ and $g_{a\gamma\gamma}^{(2)} = 2.1 \times 10^{-20} \text{ GeV}^{-1}$. These axions decay during the early Universe, injecting energy that modifies the evolution of the free electron fraction before $z \approx 10$. The resulting ionization history departs from the standard ΛCDM scenario, potentially imprinting on the CMB

polarization through the enhanced τ_{highz} . Results are shown for different values of the reheating temperature, up to the maximally allowed one, $T_{\text{reh}}^{\text{MAX}}$, defined as the value at which the computed optical depth exceeds the 2σ exclusion threshold from our τ_{highz} analysis in Paper I [34]; see Fig. 5 below.

IV. THE HIGH- z OPTICAL DEPTH

In our companion Paper I [34], we adopt a model-independent approach to constrain the optical depth τ_{reio} :

$$\tau_{\text{reio}} = \int_0^{z_{\text{max}}} \sigma_T n_e(z) \frac{dz}{(1+z)H(z)}, \quad (23)$$

where we fix $z_{\text{max}} = 800$. To better understand the contributions to the total optical depth from different epochs of reionization, we decompose τ_{reio} into two components: a low-redshift contribution τ_{lowz} and a high-redshift contribution τ_{highz} . This decomposition is particularly useful for distinguishing between standard astrophysical reionization and potential exotic energy injection scenarios that could ionize the Universe at much earlier times. Following Eq. (23), we define the optical depth at low and high redshifts in terms of a critical redshift z_c :

$$\begin{aligned} \tau_{\text{lowz}} &= \int_0^{z_c} \sigma_T n_e(z) \frac{dz}{(1+z)H(z)}, \\ \tau_{\text{highz}} &= \int_{z_c}^{z_{\text{max}}} \sigma_T n_e(z) \frac{dz}{(1+z)H(z)}, \end{aligned} \quad (24)$$

so that $\tau_{\text{reio}} = \tau_{\text{lowz}} + \tau_{\text{highz}}$.

The novelty presented in Paper I [34] consists in employing a Gaussian process (GP) method to sample random reionization histories $X_e(z)$ [34]. Using a Markov Chain Monte Carlo (MCMC) analysis with $\mathcal{O}(20)$ parameters describing the GP, and the *Planck* low- ℓ E-mode EE-only SimAll likelihood,³ we derive limits on $X_e(z)$ that extend to high redshifts. Our results yield a constraint $\tau_{\text{lowz}} = 0.0483^{+0.0083}_{-0.0080}$ at 68% confidence level (CL), and an upper limit of $\tau_{\text{highz}} < 0.108$ at 95% CL, using $z_c = 30$. Figure 5 shows the normalized posterior distribution for the high-redshift contribution to the optical depth, τ_{highz} , as derived from the *Planck* low- ℓ EE polarization data, which serves as our constraint on axion models. The distributions are largely insensitive to the choice of the critical redshift z_c , as we have demonstrated in Paper I [34]. The code used to cast the reionization results can be found at: github.com/Cheng-Hanyu/CLASS_reio_gpr.

Our GP method extends previous analyses by the *Planck* collaboration, which used similar techniques to

³ The most direct and robust probe of the reionization epoch is provided by the low- ℓ E-mode polarization data.

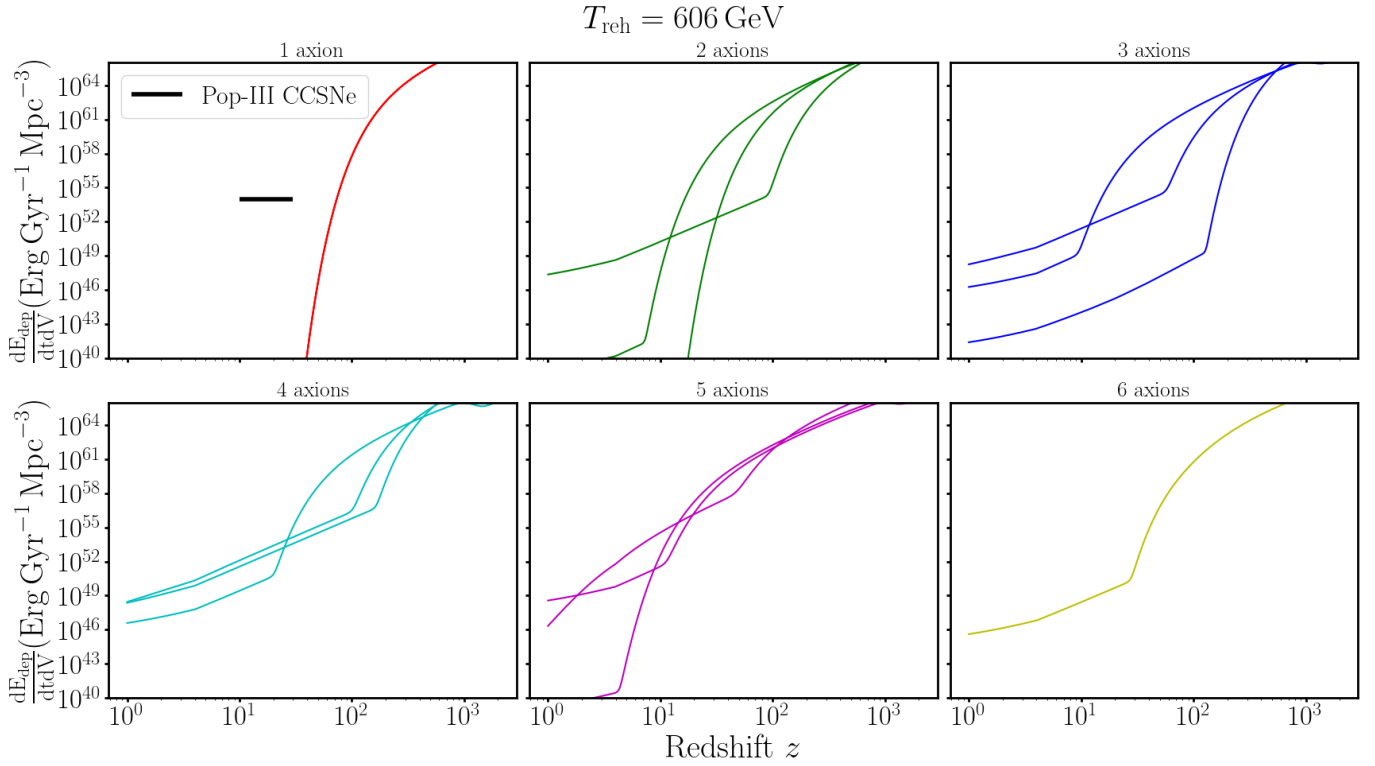


FIG. 3. The energy deposition rates from representative models with different numbers of axions in the mass window relevant for decay and ionization. Each curve corresponds to a randomly selected model from the $h^{1,1} = 50$ ensemble of Ref. [31]. The black line is, for reference, the energy injection rate and redshift range of Population III core collapse supernovae (Pop-III CCSNe) [58].

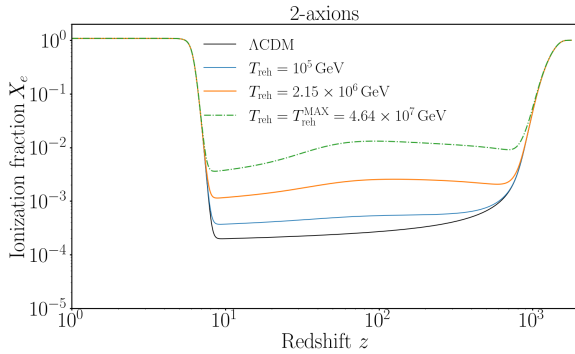


FIG. 4. **Multiple axions case.** Ionization history for a specific string axion model in an ensemble with $h^{1,1} = 50$, containing two axions within the relevant mass window. The axion parameters are: $m_a^{(1)} = 8.27 \text{ GeV}$, $g_{a\gamma\gamma}^{(1)} = 1.87 \times 10^{-20} \text{ GeV}^{-1}$, and $m_a^{(2)} = 0.72 \text{ GeV}$, $g_{a\gamma\gamma}^{(2)} = 2.1 \times 10^{-20} \text{ GeV}^{-1}$. Different line styles correspond to the reheat temperatures in the legend.

reconstruct the standard low- z reionization history [59]. Our result for $\tau_{\text{low}z}$ is consistent with their findings. In addition, the extracted posterior for $\tau_{\text{high}z}$ yields robust, model-independent constraints on exotic energy injection. By comparing theoretical predictions for $X_e(z)$ that

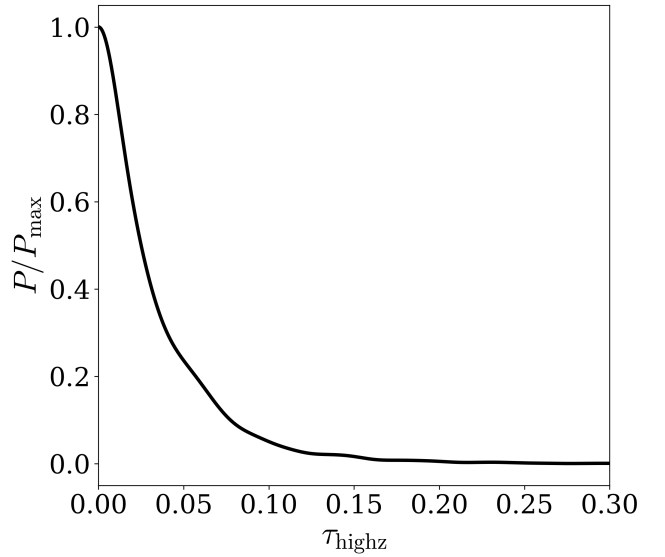


FIG. 5. Normalized posterior distribution, P/P_{max} , for the high-redshift contribution to the optical depth, for the critical redshift $z_c = 30$ defining the separation in Eq. (24). Results are based on the *Planck* low- ℓ EE dataset alone and the analysis in Paper I. This posterior distribution gives the upper limit $\tau_{\text{high}z} < 0.108$ at 95% CL, which we use to set limits on axion models.

reproduce the empirical posterior of τ_{highz} , a wide range of scenarios can be directly tested, as we demonstrate below.⁴

V. SINGLE AXION RESULTS

Before embarking on our analysis with multiple axions in string theory models, we first present constraints on the parameter space $(m_a, g_{a\gamma\gamma}, T_{\text{reh}})$ for a single-axion model. This allows us to benchmark our method against existing results in the literature and to present a new result on the maximum allowed value of T_{reh} across the axion parameter space.

Figure 6 shows the optical depth τ_{reio} in the $(m_a, g_{a\gamma\gamma})$ plane for a reheating temperature $T_{\text{reh}} = 5 \text{ MeV}$. We show three separate contours for comparison. The yellow contour shows the 2σ constraint derived from our model-independent analysis based on limits on high-redshift energy injection, labeled τ_{highz} [34]. The red contour corresponds to the exclusion derived by comparing the total optical depth τ_{reio} to the *Planck* constraint, assuming standard low-redshift reionization only, denoted τ_{lowz} . For reference, the blue contour reproduces the bound from Ref. [17]. Our analysis demonstrates that our model-independent treatment accurately reproduces the limits from previous work [17, 35], while being only marginally more conservative. In contrast, using the full τ_{reio} constraint without accounting for the standard low-redshift reionization history leads to overly conservative exclusions.

We have thus validated two key elements of our pipeline: (i) our freeze-in fits [36], which are consistent with the relic abundance calculations in Ref. [17]; and (ii) our model-independent CMB analysis of the ionization history, which leads to the τ_{highz} posterior and agrees with the results obtained using the “on-the-spot” approximation developed in Ref. [35].

The on-the-spot approximation, relevant for general decaying dark matter scenarios, assumes that: (i) energy from decay is deposited instantaneously into photons; and (ii) the efficiency of the energy deposition follows a simple exponential decay law, given by

$$f(z) = f_{\text{eff}} e^{-t(z)\Gamma}, \quad (25)$$

where f_{eff} depends only on m_χ and its decay channels, and is defined in [35]. These models are specified by three parameters: the decay rate Γ , the DM fraction in the decaying species \mathcal{F} , and the mass of the decaying DM component m_χ .

Under the assumptions of the on-the-spot approximation, constraints from CMB anisotropies are obtained by performing MCMC analyses for each set of values

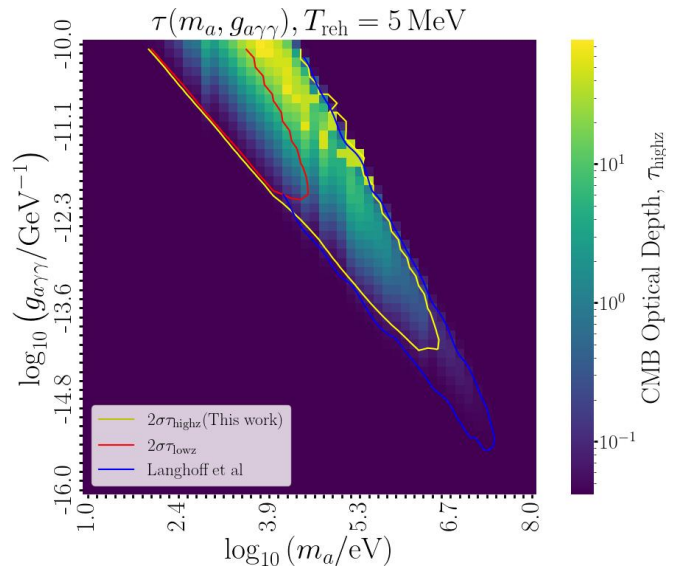


FIG. 6. Optical depth τ_{highz} (vertical color scaling) as a function of the axion mass (horizontal axis) and axion–photon coupling (vertical axis). Solid lines denote 95% CL (2σ) exclusion contours from different analyses. The yellow line shows constraints from our high-redshift optical depth estimation using GP regression results marginalized over $z \in [30, 800]$. The red line represents low-redshift constraints marginalized over $z \in [0, 30]$ from our GP regression analysis, which are consistent with the optical depth estimation from the *Planck* 2018 result [59]. The blue line shows CMB anisotropy constraints from Ref. [17], labeled “Langhoffer et al.” See details about the GP regression and MCMC analysis in Paper I [34].

(m_χ, Γ^{-1}) , using flat priors on the six ΛCDM parameters plus \mathcal{F} , and deriving upper limits on \mathcal{F} from the data. When applied to axions, this approach yields the fits presented in Ref. [17], whose workflow is conceptually and operationally distinct from the one we adopt in this work. Ref. [17] is based on Ref. [35] and uses more CMB likelihoods than we employ (temperature in addition to polarization), which explains the slightly stronger limit under the same assumptions of relativistic axions. However, in Appendix A, we extend our assumptions to include effects when $m_a \approx T_{\text{reh}}$, which suggest that the correct limit does not extend to as high mass / low coupling as the tail end of the Ref. [17] contour in Fig. 6.

We now apply our method to compute a new result, so far as we are aware, for a single axion: the maximum reheating temperature $T_{\text{reh}}^{\text{MAX}}$ allowed across the $(m_a, g_{a\gamma\gamma})$ parameter space. For a given axion mass and photon coupling, we calculate the high-redshift optical depth τ_{highz} as a function of reheating temperature, using the freeze-in abundance as input. Figure 7 shows this dependence for a representative selection of single-axion models, as indicated in the legend. The gray dashed line indicates the 2σ upper bound on τ_{highz} derived in Paper I (and shown in Fig. 5), which sets the exclusion threshold. As T_{reh} increases, the freeze-in abundance grows, resulting in an increase in τ_{highz} . For each model, we identify the

⁴ In Paper I [34], we validate this approach with a direct χ^2 comparison using the *Planck* low- ℓ EE-only SimAll likelihood.

point at which τ_{highz} crosses the exclusion threshold: this defines the corresponding maximum reheating temperature $T_{\text{reh}}^{\text{MAX}}$ allowed by current data. For comparison, the black dashed line shows the value $\tau_{\text{highz}} = 0.0407$, obtained from the baseline ΛCDM scenario with $z_c = 30$ in Eq. (24).

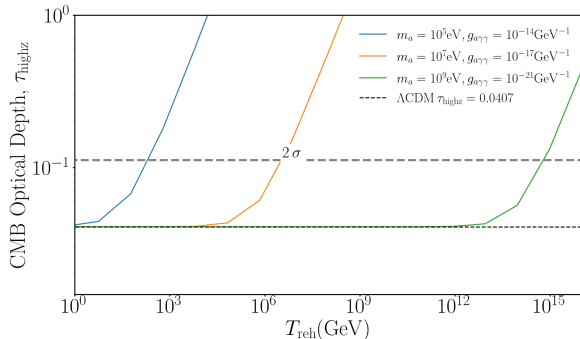


FIG. 7. The optical depth τ_{highz} as a function of reheating temperature, for a selection of single-axion models with varying mass and photon coupling. The gray dashed line marks the 2σ upper limit on τ_{highz} derived in Paper I (see also Fig. 5), while the black dashed line shows the ΛCDM contribution (see main text for details). The intersection of each curve with the gray dashed line defines the maximum reheating temperature $T_{\text{reh}}^{\text{MAX}}$ allowed for that model.

Figure 8 shows the maximum reheating temperature $T_{\text{reh}}^{\text{MAX}}$ allowed by CMB optical depth constraints, mapped over the $(m_a, g_{a\gamma\gamma})$ parameter space for a single axion-like particle. For each point in this plane, we compute the freeze-in abundance and the resulting high-redshift optical depth τ_{highz} , identifying the highest reheating temperature for which the predicted τ_{highz} remains below the 2σ exclusion threshold. Our procedure smoothly interpolates between two limiting cases: the low-reheating bound from Ref. [17], evaluated at $T_{\text{reh}} = T_{\text{BBN}}$, and the fully thermalized limit from Refs. [13, 46], corresponding to $T_{\text{reh}} \sim 10^{16}$ GeV. Contours of constant $T_{\text{reh}}^{\text{MAX}}$ are overlaid to indicate the energy scale at which each region of parameter space becomes excluded. This figure thus serves as a direct map between axion properties and the maximum cosmologically allowed reheating temperature. Notably, the lower-right region of the parameter space permits high-scale reheating, in agreement with constraints from inflationary gravitational wave backgrounds [60], while the upper-right region is unconstrained in our analysis, as axion decays occur before recombination and leave no imprint on the ionization history.

VI. CONSTRAINTS ON REHEATING IN STRING THEORY

We now turn to a quantitative assessment of the constraints that can be placed within the string axiverse.

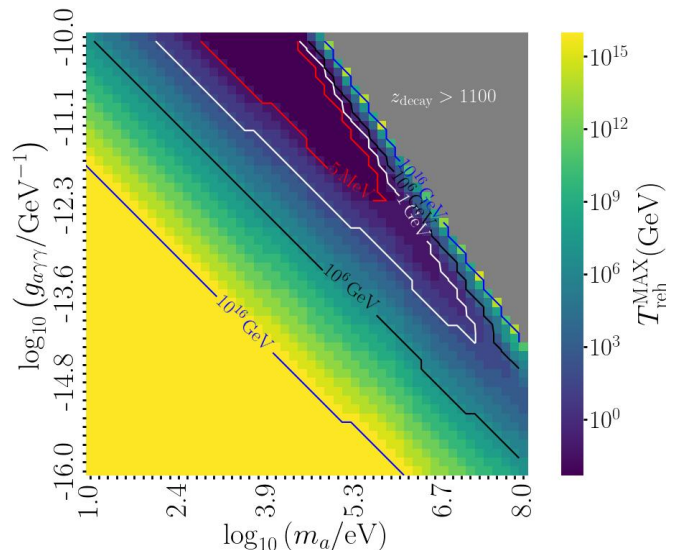


FIG. 8. The maximum reheating temperature $T_{\text{reh}}^{\text{MAX}}$ allowed by CMB optical depth constraints, shown as a function of m_a and $g_{a\gamma\gamma}$ for a single axion-like particle. Solid contours indicate constant values of $T_{\text{reh}}^{\text{MAX}}$: 5 MeV (red), 1 GeV (white), 10^6 GeV (black), and 10^{16} GeV (blue). The lower-left region of the plot is compatible with high reheating temperatures, including values near $\sim 10^{16}$ GeV, consistent with expectations from inflationary gravitational wave constraints [60]. The gray upper-right region is unconstrained by our analysis, as the axion decays before recombination and thus does not contribute to the high-redshift optical depth (see Ref. [16] for constraints in this region).

We generate ensembles of models as described above, using the methodology of Ref. [31]. Figure 9 shows the axion decay temperature, T_{decay} , and the corresponding freeze-in relic abundance fraction prior to decay, \mathcal{F}_a , for the ensemble with $h^{1,1} = 50$, to provide a preliminary estimate of the expected constraints. Existing limits on single axion decays from the CMB optical depth exclude regions with $T_{\text{decay}} \lesssim 1$ eV and $\mathcal{F}_a \gtrsim 10^{-10}$ [17, 35]. From the figure, it appears that a subset of models within the ensemble enter this excluded region, particularly for $T_{\text{reh}} \gtrsim 10^{10}$ GeV [31], indicating potential tension with observational bounds. The following section quantifies this tension precisely.

Each model contains many axions, spanning a broad range of masses and decay constants. We preprocess the ensembles to ensure both the accuracy of the numerical results and computational feasibility. Specifically, we define a mass window from 10^5 eV to 10^{10} eV, and select at most 10 axions per model within this window for further analysis. This selection is justified by the expected axion mass hierarchies and the approximately uniform coupling to photons (for axions above the “light threshold” mass, which typically holds for high-mass axions), which together ensure that only a small number of axions significantly contribute to the CMB optical depth. This preprocessing step reduces the number of models

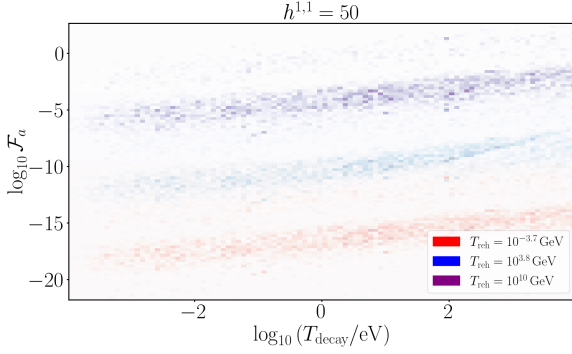


FIG. 9. 2D histogram of the decay temperature and relic abundance of string axions with $h^{1,1} = 50$, shown as a function of the freeze-in relic abundance fraction \mathcal{F}_a and the decay temperature T_{decay} . Each color bin corresponds to a different reheating temperature. The correlation between \mathcal{F}_a and T_{decay} arises from the dependence of the freeze-in abundance and decay rates on the axion parameters m_a and $g_{a\gamma\gamma}$, as given in Eqs. (6) and (9).

that must be evaluated. Empirically, the number of axions within this window rarely exceeds 10 even prior to truncation, so this selection does not bias the physical results.

For all selected axions in a given model, we then compute the freeze-in abundance and evaluate the optical depth τ_{highz} from their decay, using the methods of Sec. III. To avoid numerical instabilities from unphysically large values of the optical depth during the calculations, we set an upper limit $\tau_{\text{highz}} \leq 1$. Figure 10 shows the distribution of τ_{highz} for models with $h^{1,1} = 50$, for different reheating temperatures. The red dashed line indicates the 2σ exclusion threshold derived from our posterior analysis of τ_{highz} . For each model, we identify the maximum reheating temperature $T_{\text{reh}}^{\text{MAX}}$ at which the model remains consistent with this threshold.

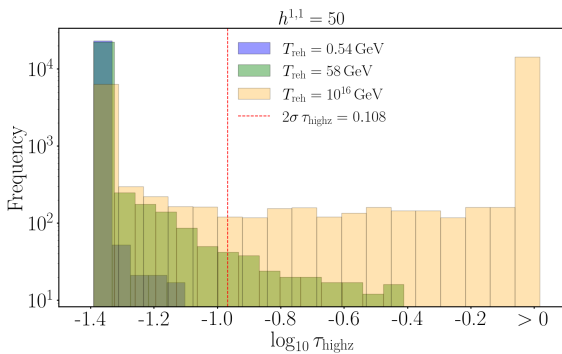


FIG. 10. Distribution of the high-redshift optical depth τ_{highz} for string axion models with $h^{1,1} = 50$. The red dashed line indicates the 2σ exclusion threshold, corresponding to $\tau_{\text{highz}} < 0.108$, based on our data analysis as described in Paper I.

Our final results are displayed in Fig. 11, where we show the fraction of excluded string theory models in our ensemble as a function of the reheating temperature T_{reh} for Hodge numbers $h^{1,1} = 20, 50, 100$. For $h^{1,1} = 20, 50$, we find that up to 25% of models are excluded at the largest value of $T_{\text{reh}} \approx 10^{16}$ GeV, and around 15% of models are excluded for $T_{\text{reh}} \gtrsim 10^{10}$ GeV. At $h^{1,1} = 100$, the constraints are weaker: while the maximum axion-photon coupling increases with $h^{1,1}$, the well-coupled axions also become lighter, due to “kinetic isolation” and the “light threshold”, as described in Ref. [31].

The results in Fig. 11 use the more accurate Kähler cone \mathcal{K}_U , which improves over the computation in Ref. [31], which used \mathcal{K}_V . Constraints using \mathcal{K}_U , where it can be computed with present methods, are stronger compared to \mathcal{K}_V due to the presence of more small divisors in \mathcal{K}_U . We expect, furthermore, that the accuracy of the Kähler cone becomes more important at large $h^{1,1}$, and thus further work is required to place explicit constraints in this important part of the landscape [61].

VII. CONCLUSIONS

We have developed a robust and efficient pipeline to evaluate the impact of decaying string axions on the high-redshift CMB optical depth, τ_{highz} , which is a sensitive probe of light decaying relics. The string axiverse effective field theories derived from type IIB Calabi-Yau orientifold compactifications contain $h^{1,1}$ axions. We constructed explicit models using CYTOOLS [27], following Ref. [31], at $h^{1,1} = 20, 50, 100$. For each model and axion, we computed the freeze-in abundance [36] and, using the methods developed in the current paper and a modified version of DARKHISTORY [37], calculated the full ionization history $X_e(z)$ for simultaneous decays of all axions. We then derived τ_{highz} and, following Paper I [34], imposed a conservative exclusion threshold of $\tau_{\text{highz}} < 0.108$ (95% CL). This allowed us to determine the fraction of excluded models in the axiverse ensemble as a function of the reheating temperature. At $h^{1,1} = 20, 50, 100$, we found that 15%, 15%, and 10% of models prefer a reheating temperature $T_{\text{reh}} \lesssim 10^{10}$ GeV at 95% CL using our model-independent test.

We have focused on axion-photon interactions and neglected axion couplings to fermions, which are assumed to be subdominant in the region of parameter space considered. Extensions of this analysis could include axion-fermion couplings, which would modify the production mechanisms and open additional decay channels into Standard Model particles, which later branch into electrons. In fact, significant progress has been made in recent years on fermion-driven axion production [62–66], making such an extension viable once axion-fermion couplings can be computed in ensembles of compactifications of type IIB string theory. Note, however, that these couplings are model-dependent and may be suppressed compared to axion-photon interactions [25, 67].

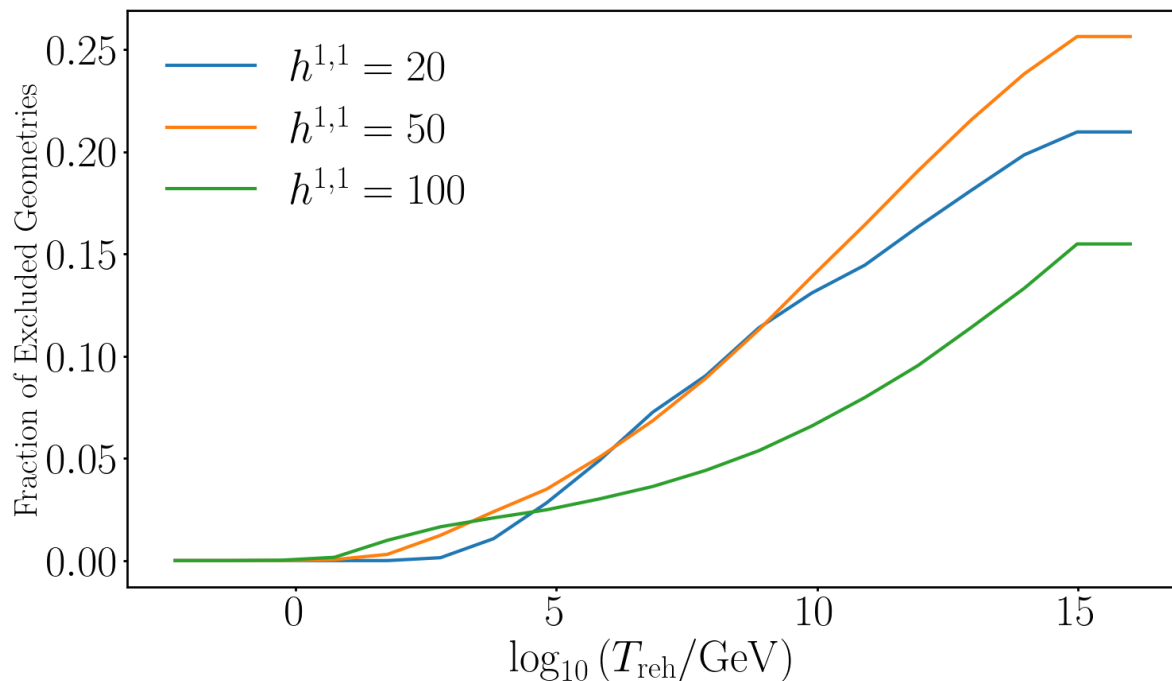


FIG. 11. Fraction of excluded string theory models at 95% CL as a function of the reheating temperature T_{reh} for different Hodge numbers $h^{1,1}$. Models are constructed as described in Sec. II, following Ref. [31], using CYTOOLS [27]. The relic abundance is computed following Ref. [36]. The full ionization history is evaluated using the methods described in this paper, in conjunction with DARKHISTORY [37]. Constraints are derived from the CMB optical depth, following the model-independent analysis presented in Paper I [34].

In particular, they depend on a computation of matter couplings in the Kähler potential. Nevertheless, axion couplings to fermion fields are generically induced at loop level from the axion-photon coupling.

In the present work, we have used a single observable, namely the high- z CMB optical depth upper limit derived in Paper I [34], to exclude a small but significant fraction of string theory models with high-temperature reheating. The same underlying physics of the axion, freeze-in production followed by decay, also affects several other observables, including X-ray line searches, big bang nucleosynthesis, and CMB spectral distortions [16, 17], all of which could be used to further constrain the axiverse [31]. However, just as we here developed a new calculation of the ionization state of the Universe, including multi-axion energy injection, to properly compute the CMB optical depth constraint, so exploiting these additional datasets will require new calculations that include multi-axion decays. Incorporating additional observables alongside the CMB optical depth will greatly extend the range of string theory models that can be constrained in models with high-temperature reheating.

ACKNOWLEDGMENTS

HC, ZY, LV acknowledge support by the National Natural Science Foundation of China (NSFC) through the grant No. 12350610240 “Astrophysical Axion Laboratories”. This publication is based upon work from the COST Actions “COSMIC WISPerS” (CA21106) and “Addressing observational tensions in cosmology with systematics and fundamental physics (CosmoVerse)” (CA21136), both supported by COST (European Cooperation in Science and Technology). HC, ZY acknowledge the support of the China Scholarship Council program (Project ID:202406230341 and 202406230357). EDV is supported by a Royal Society Dorothy Hodgkin Research Fellowship. DJEM is supported by an Ernest Rutherford Fellowship from the Science and Technologies Facilities Council, STFC (Grant No. ST/T004037/1), an STFC consolidator grant (Grant No. ST/X000753/1) and by a Leverhulme Trust Research Project (Grant No. RPG-2022-145). NG is supported in part by a grant from the Simons Foundation (602883,CV) and gifts from the DellaPietra Foundation. LV also thanks Istituto Nazionale di Fisica Nucleare (INFN) through the “QGSKY” Iniziativa Specifica project. LV additionally thanks the Tsung-Dao Lee Institute for hospitality during the final stages

of this work. We are grateful to Mudit Jain for providing assistance with the fits used for the Freeze-in calculation, to Sebastian Vander Ploeg Fallon for investigating the dependence of axion spectra on different approximations to the Kähler cone, to Miguel Escudero for correspondence

about the baryon temperature, and Liam McAllister and Jakob Moritz for discussions. This work made use of the open source software MATPLOTLIB [68], NUMPY [69], and SCIPY [70].

-
- [1] R. D. Peccei and H. R. Quinn, *Phys. Rev. Lett.* **38**, 1440 (1977).
 - [2] R. D. Peccei and H. R. Quinn, *Phys. Rev. D* **16**, 1791 (1977).
 - [3] S. Weinberg, *Phys. Rev. Lett.* **40**, 223 (1978).
 - [4] F. Wilczek, *Phys. Rev. Lett.* **40**, 279 (1978).
 - [5] L. F. Abbott and P. Sikivie, *Phys. Lett. B* **120**, 133 (1983).
 - [6] M. Dine and W. Fischler, *Phys. Lett. B* **120**, 137 (1983).
 - [7] J. Preskill, M. B. Wise, and F. Wilczek, *Phys. Lett. B* **120**, 127 (1983).
 - [8] D. J. E. Marsh, *Phys. Rept.* **643**, 1 (2016), [arXiv:1510.07633 \[astro-ph.CO\]](#).
 - [9] L. Di Luzio, M. Giannotti, E. Nardi, and L. Visinelli, *Phys. Rept.* **870**, 1 (2020), [arXiv:2003.01100 \[hep-ph\]](#).
 - [10] F. Chadha-Day, J. Ellis, and D. J. E. Marsh, *Sci. Adv.* **8**, abj3618 (2022), [arXiv:2105.01406 \[hep-ph\]](#).
 - [11] C. A. J. O’Hare, *PoS COSMICWISPerS*, 040 (2024), [arXiv:2403.17697 \[hep-ph\]](#).
 - [12] E. Masso, F. Rota, and G. Zsembinski, *Phys. Rev. D* **66**, 023004 (2002), [arXiv:hep-ph/0203221](#).
 - [13] D. Cadamuro and J. Redondo, *JCAP* **02**, 032 (2012), [arXiv:1110.2895 \[hep-ph\]](#).
 - [14] P. Arias, D. Cadamuro, M. Goodsell, J. Jaeckel, J. Redondo, and A. Ringwald, *JCAP* **06**, 013 (2012), [arXiv:1201.5902 \[hep-ph\]](#).
 - [15] B. Bolliet, F. Chluba, and R. Battye, *Mon. Not. Roy. Astron. Soc.* **507**, 3148 (2021), [arXiv:2012.07292 \[astro-ph.CO\]](#).
 - [16] C. Balázs *et al.*, *JCAP* **12**, 027 (2022), [arXiv:2205.13549 \[astro-ph.CO\]](#).
 - [17] K. Langhoff, N. J. Outmezguine, and N. L. Rodd, *Phys. Rev. Lett.* **129**, 241101 (2022), [arXiv:2209.06216 \[hep-ph\]](#).
 - [18] F. Capozzi, R. Z. Ferreira, L. Lopez-Honorez, and O. Mena, *JCAP* **06**, 060 (2023), [arXiv:2303.07426 \[astro-ph.CO\]](#).
 - [19] H. Liu, W. Qin, G. W. Ridgway, and T. R. Slatyer, *Phys. Rev. D* **108**, 043531 (2023), [arXiv:2303.07370 \[astro-ph.CO\]](#).
 - [20] E. Witten, *Phys. Lett. B* **149**, 351 (1984).
 - [21] P. Svrcek and E. Witten, *JHEP* **06**, 051 (2006), [arXiv:hep-th/0605206](#).
 - [22] J. P. Conlon, *JHEP* **05**, 078 (2006), [arXiv:hep-th/0602233](#).
 - [23] A. Arvanitaki, S. Dimopoulos, S. Dubovsky, N. Kaloper, and J. March-Russell, *Phys. Rev. D* **81**, 123530 (2010), [arXiv:0905.4720 \[hep-th\]](#).
 - [24] B. S. Acharya, K. Bobkov, and P. Kumar, *JHEP* **11**, 105 (2010), [arXiv:1004.5138 \[hep-th\]](#).
 - [25] M. Cicoli, M. Goodsell, and A. Ringwald, *JHEP* **10**, 146 (2012), [arXiv:1206.0819 \[hep-th\]](#).
 - [26] M. Demirtas, C. Long, L. McAllister, and M. Stillman, *JHEP* **04**, 138 (2020), [arXiv:1808.01282 \[hep-th\]](#).
 - [27] M. Demirtas, A. Rios-Tascon, and L. McAllister, (2022), [arXiv:2211.03823 \[hep-th\]](#).
 - [28] E. Sheridan, F. Carta, N. Gendler, M. Jain, D. J. E. Marsh, L. McAllister, N. Righi, K. K. Rogers, and A. Schachner, (2024), [arXiv:2412.12012 \[hep-th\]](#).
 - [29] V. M. Mehta, M. Demirtas, C. Long, D. J. E. Marsh, L. McAllister, and M. J. Stott, *JCAP* **07**, 033 (2021), [arXiv:2103.06812 \[hep-th\]](#).
 - [30] M. Demirtas, N. Gendler, C. Long, L. McAllister, and J. Moritz, *JHEP* **06**, 092 (2023), [arXiv:2112.04503 \[hep-th\]](#).
 - [31] N. Gendler, D. J. E. Marsh, L. McAllister, and J. Moritz, *JCAP* **09**, 071 (2024), [arXiv:2309.13145 \[hep-th\]](#).
 - [32] N. Gendler and D. J. E. Marsh, *Phys. Rev. Lett.* **134**, 081602 (2025), [arXiv:2407.07143 \[hep-th\]](#).
 - [33] J. N. Benabou, K. Fraser, M. Reig, and B. R. Safdi, (2025), [arXiv:2505.15884 \[hep-ph\]](#).
 - [34] H. Cheng, Z. Yin, E. Di Valentino, D. J. E. Marsh, and L. Visinelli, (2025), [arXiv:2506.19096 \[astro-ph.CO\]](#).
 - [35] V. Poulin, J. Lesgourgues, and P. D. Serpico, *JCAP* **03**, 043 (2017), [arXiv:1610.10051 \[astro-ph.CO\]](#).
 - [36] M. Jain, A. Maggi, W.-Y. Ai, and D. J. E. Marsh, *JHEP* **11**, 166 (2024), [Erratum: *JHEP* **04**, 156 (2025)], [arXiv:2406.01678 \[hep-ph\]](#).
 - [37] H. Liu, G. W. Ridgway, and T. R. Slatyer, *Phys. Rev. D* **101**, 023530 (2020), [arXiv:1904.09296 \[astro-ph.CO\]](#).
 - [38] R. Petrossian-Byrne and G. Villadoro, (2025), [arXiv:2503.16387 \[hep-ph\]](#).
 - [39] T. W. Grimm and J. Louis, *Nucl. Phys. B* **699**, 387 (2004), [arXiv:hep-th/0403067](#).
 - [40] M. Cicoli, A. Schachner, and P. Shukla, *JHEP* **04**, 003 (2022), [arXiv:2109.14624 \[hep-th\]](#).
 - [41] L. McAllister and F. Quevedo, (2023), [arXiv:2310.20559 \[hep-th\]](#).
 - [42] L. McAllister, J. Moritz, R. Nally, and A. Schachner, *Phys. Rev. D* **111**, 086015 (2025), [arXiv:2406.13751 \[hep-th\]](#).
 - [43] V. V. Batyrev, *J. Alg. Geom.* **3**, 493 (1994), [arXiv:alg-geom/9310003](#).
 - [44] M. Kreuzer and H. Skarke, *Adv. Theor. Math. Phys.* **4**, 1209 (2000), [arXiv:hep-th/0002240](#).
 - [45] J. Moritz, (2023), [arXiv:2305.06363 \[hep-th\]](#).
 - [46] D. Cadamuro, S. Hannestad, G. Raffelt, and J. Redondo, *JCAP* **02**, 003 (2011), [arXiv:1011.3694 \[hep-ph\]](#).
 - [47] L. J. Hall, K. Jedamzik, J. March-Russell, and S. M. West, *JHEP* **03**, 080 (2010), [arXiv:0911.1120 \[hep-ph\]](#).
 - [48] P. F. de Salas, M. Lattanzi, G. Mangano, G. Miele, S. Pastor, and O. Pisanti, *Phys. Rev. D* **92**, 123534 (2015), [arXiv:1511.00672 \[astro-ph.CO\]](#).
 - [49] T. Hasegawa, N. Hiroshima, K. Kohri, R. S. L. Hansen, T. Tram, and S. Hannestad, *JCAP* **12**, 012 (2019), [arXiv:1908.10189 \[hep-ph\]](#).
 - [50] N. Aghanim *et al.* (Planck), *Astron. Astrophys.* **641**, A6 (2020), [Erratum: *Astron. Astrophys.* **652**, C4 (2021)],

- arXiv:1807.06209 [astro-ph.CO].
- [51] J. Jaeckel, J. Redondo, and A. Ringwald, *Phys. Rev. D* **89**, 103511 (2014), arXiv:1402.7335 [hep-ph].
 - [52] L. Visinelli and P. Gondolo, *Phys. Rev. D* **81**, 063508 (2010), arXiv:0912.0015 [astro-ph.CO].
 - [53] M. Escudero, C. K. Pooni, M. Fairbairn, D. Blas, X. Du, and D. J. E. Marsh, *Phys. Rev. D* **109**, 043018 (2024), arXiv:2302.10206 [hep-ph].
 - [54] T. R. Slatyer and C.-L. Wu, *Phys. Rev. D* **95**, 023010 (2017), arXiv:1610.06933 [astro-ph.CO].
 - [55] M. Lucca, N. Schöneberg, D. C. Hooper, J. Lesgourgues, and J. Chluba, *JCAP* **02**, 026 (2020), arXiv:1910.04619 [astro-ph.CO].
 - [56] B. D. Fields, K. A. Olive, T.-H. Yeh, and C. Young, *JCAP* **03**, 010 (2020), [Erratum: *JCAP* **11**, E02 (2020)], arXiv:1912.01132 [astro-ph.CO].
 - [57] C. Heinrich and W. Hu, *Phys. Rev. D* **104**, 063505 (2021), arXiv:2104.13998 [astro-ph.CO].
 - [58] T. Hartwig *et al.*, *Astrophys. J.* **936**, 45 (2022), arXiv:2206.00223 [astro-ph.GA].
 - [59] N. Aghanim *et al.* (Planck), *Astron. Astrophys.* **641**, A1 (2020), arXiv:1807.06205 [astro-ph.CO].
 - [60] V. Domcke and J. Heisig, *Phys. Rev. D* **92**, 103515 (2015), arXiv:1504.00345 [astro-ph.CO].
 - [61] M. Demirtas, L. McAllister, and A. Rios-Tascon, *Fortsch. Phys.* **68**, 2000086 (2020), arXiv:2008.01730 [hep-th].
 - [62] F. Arias-Aragón, F. D'Eramo, R. Z. Ferreira, L. Merlo, and A. Notari, *JCAP* **03**, 090 (2021), arXiv:2012.04736 [hep-ph].
 - [63] L. Caloni, M. Gerbino, M. Lattanzi, and L. Visinelli, *JCAP* **09**, 021 (2022), arXiv:2205.01637 [astro-ph.CO].
 - [64] F. D'Eramo, E. Di Valentino, W. Giarè, F. Hajkarim, A. Melchiorri, O. Mena, F. Renzi, and S. Yun, *JCAP* **09**, 022 (2022), arXiv:2205.07849 [astro-ph.CO].
 - [65] F. D'Eramo, A. Lenoci, and A. Dekker, (2025), arXiv:2506.13864 [hep-ph].
 - [66] N. Barbieri, T. Brinckmann, S. Gariazzo, M. Lattanzi, S. Pastor, and O. Pisanti, (2025), arXiv:2501.01369 [astro-ph.CO].
 - [67] J. Halverson, C. Long, and P. Nath, *Phys. Rev. D* **96**, 056025 (2017), arXiv:1703.07779 [hep-ph].
 - [68] J. D. Hunter, *Computing in Science and Engineering* **9**, 90 (2007).
 - [69] C. R. Harris *et al.*, *Nature (London)* **585**, 357 (2020), arXiv:2006.10256 [cs.MS].
 - [70] P. Virtanen *et al.*, *Nature Methods* **17**, 261 (2020), arXiv:1907.10121 [cs.MS].

Appendix A: Validity of relativistic freeze-in abundance approach

A population of axions with mass m_a , produced by freeze-in from the interaction with a thermal bath at temperature T_{reh} , has number density

$$n_{\text{eq}} = \frac{1}{2\pi^2} \int_0^\infty \frac{p^2}{e^{\sqrt{p^2 + m_a^2}/T_{\text{reh}}} - 1} dp. \quad (\text{A1})$$

This number density enters the definition of the DM fraction in Eq. (9). In the relativistic limit $m_a \ll T_{\text{reh}}$, Eq. (9) can be approximated as

$$n_{\text{eq}} \approx \frac{\xi(3)}{\pi^2} T_{\text{reh}}^3, \quad (\text{A2})$$

which leads to the simplified expression in Eq. (10), used throughout our analysis. In this appendix, we compare the freeze-in abundance results shown in Fig. 6 to those obtained using the complete, un-approximated, number density in Eq. (A1). The results, shown in Fig. 12, indicate that the two methods lead to consistent constraints, with the full treatment (white solid line) resulting in slightly more conservative bounds than the approximation used in the main text (yellow solid line). Notably, the full treatments present a cutoff in the mass range around $m_a \sim T_{\text{reh}}$, which in the exact case arises from the exponential suppression in the phase-space distribution. Since the approximate expression reproduces this cutoff in the constrained value of $(m_a, g_{a\gamma\gamma})$ sufficiently accurately, its use is justified in our study with large ensembles due to the reduced computational cost. Consequently, we do not expect the constraint to be valid for axion masses significantly above T_{reh} , contrary to what is reported in Ref. [17], see the blue contours in Fig. 12.

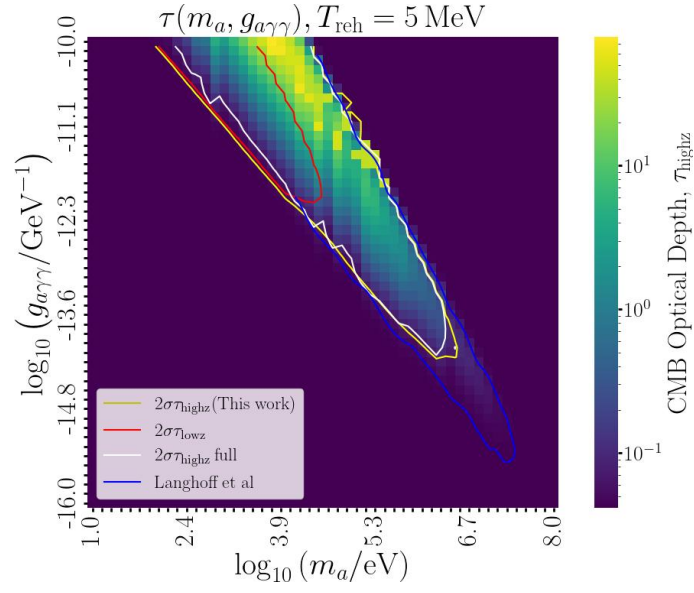


FIG. 12. Optical depth τ_{highz} (vertical color scale) as a function of the axion mass (horizontal axis) and axion-photon coupling (vertical axis). Solid lines denote 95% CL exclusion contours from different methods. The solid white line shows the exclusion limit derived by using the full integral expression for the equilibrium number density n_{eq} . The other contours are the same as those shown in Fig. 6.